Available online at www.sciencedirect.com
ScienceDirect
Trans. Nonferrous Met. Soc. China 34(2024) 769−785
Transactions of Nonferrous Metals Society of China
www.tnmsc.cn

Enhancing corrosion resistance of $Al_{50}Ni_{50}$ alloy by increasing cooling rate plus annealing

Han-ze LIU[1], Zhi-cheng YAN[1], Qi CHEN[1], Hao ZHANG[1], Yu FENG[1], Zhi-gang QI[1], Zhao-xuan WANG[1], Shao-peng PAN[2], Yi-yong JIA[3], Wei-min WANG[1]

1. Key Laboratory for Liquid-Solid Structural Evolution and Processing of Materials (Ministry of Education), School of Materials Science and Engineering, Shandong University, Jinan 250061, China;
2. College of Materials Science and Engineering, Taiyuan University of Technology, Taiyuan 030002, China;
3. Londerful New Materials (Heze) Co., Ltd., Heze 274000, China

Received 28 August 2022; accepted 22 March 2023

Abstract: Monophasic $Al_{50}Ni_{50}$ ribbons were fabricated by melt spinning at circumferential speeds (S_c) of 21 and 42 m/s, and subsequently annealed at various temperatures. The microstructure and corrosion behavior of ribbons were studied through various experimental methods. With increasing S_c, the as-spun and annealed ribbons at 42 m/s show a higher (100) crystal orientation factor $F_{(100)}$, a lower barrier to recrystallization and a higher total film resistance than the counterparts with 21 m/s. The as-spun ribbon at 42 m/s demonstrated a denser and more stable Al_2O_3 passive film compared to the as-spun and annealed ribbons at 21 m/s. This improvement in passive film can be further enhanced by 700 °C annealing. Therefore, the corrosion resistance of AlNi ribbons can be improved by increasing S_c and additional annealing at an appropriate temperature.

Key words: AlNi alloy; rapid solidification; orientation factor; recrystallization; corrosion behavior

1 Introduction

AlNi alloys, including nickel aluminides, have recently garnered significant attention from both scientists and industries due to their advantageous properties, such as small atoms density, high compression resistance, and high antioxidant capacity [1−5]. Nickel aluminides appear to have very good properties that make them eligible for the development of new materials. They have excellent oxidation resistance, thermal stability and strength at high temperature [6,7]. Among the AlNi alloys, the AlNi phase stands out as the most promising, exhibiting a relatively low density of 5910 kg/m^3, a melting point of 1638 °C, excellent corrosion resistance, and good thermal conductivity of 75 W/(m·K). These desirable properties make it a suitable material for a wide range of engineering applications, including the coating of materials such as surface catalysts and semiconductors to impart corrosion resistance, as well as for use in structural applications such as turbine blades and vanes in the automotive and aeronautical industries where lightweight components are in high demand [8−11].

Rapid solidification (RS) technologies have been defined as the rapid dissipation of thermal energy during the transition from a liquid state at high temperatures to a solid state at ambient temperature [12]. Rapid solidification technologies for liquid metal, together with appropriate selection of the chemical composition of aluminum alloys, make it possible to obtain metallic materials with unique structures and different properties compared with the conventional materials with an ordered crystalline structure [13−16]. According to the

Corresponding author: Wei-min WANG, Tel: +86-531-88392749, E-mail: weiminw@sdu.edu.cn
DOI: 10.1016/S1003-6326(23)66433-7

literature, for the process to be classified as rapid solidification, the critical cooling rate must be exceeded [17]. The classification of rapid solidification can be considered further by taking into account the form of obtained samples (for example, powder techniques), the obtained structure (grain size, particle size), and the cooling rate [18−20]. In order to obtain high-quality aluminum alloys for structural applications, a number of parameters should be taken into account, namely, chemical composition, atomic diameters, atomic vapor interactions, and liquid temperature [7,21−23]. The most common rapid solidification technologies include water quenching, high-pressure casting, pressure casting into a copper mold, and continuous casting methods such as melting spinning [16]. In the melt spinning process, a higher circumferential speed (S_c) corresponds to a higher cooling rate, according to Ref. [24].

Recrystallization is a critical process in the thermomechanical processing of metals, as it facilitates the restoration of a worked metal to an unworked and formable state [25]. In the annealing process as the temperature beyond certain value, the deformed grains of the crystal structure are replaced by a new set of stress-free grains that nucleate and recrystallize until all the original grains have been consumed. This process can eliminate all the effects of strain hardening in steel such as heavy plastic deformation produced during cold working [26,27]. When temperature is raised, the new, stress-free grains nucleate and grow inside the old deformed grains and also at the grain boundaries. This replaces the distorted grains produced by strain hardening. The mechanical properties of metal revert back to their original, more ductile and weaker state [28,29].

Currently, while the relationship between the mechanical properties and crystal structure of alloys has been extensively studied [30,31], the influence of crystal orientation on the corrosion behavior of metallic materials and the underlying reaction mechanisms are not yet fully understood. To further understand the corrosion mechanism of the alloy, it is important to study the corrosion behavior of the matrix phase with different orientations. Recently, the differences in the corrosion resistance of single-crystal aluminium with different crystal orientations have been investigated in neutral and acidic solutions [32−34]. It was discovered that the corrosion resistance of the (100) crystalline surface was superior to that of other crystalline surfaces. Hence, in order to further verify the variation of the (100) crystal orientation, the orientation factor $F_{(100)}$ of AlNi ribbon is valuable to be checked in both the as-spun and annealed samples.

The objective of this study is to investigate the effect of cooling rate and annealing process on the microstructure and corrosion properties of single phase $Al_{50}Ni_{50}$ alloys. The microstructure and corrosion behavior of as-spun and annealed $Al_{50}Ni_{50}$ ribbons at different cooling rates were examined using various experimental techniques. The findings of this study provide a promising approach for enhancing the corrosion resistance of Al- or Ni-based alloys.

2 Experimental

2.1 Sample preparation

The $Al_{50}Ni_{50}$ ingots were produced via melting 99.99% Al and 99.99% Ni in a vacuum arc furnace (Ebmund Büehler, MAM−1). The arc melting system was initially vacuumed to be 5.0×10^{-3} Pa and then filled with purified argon (99.999%). 4 g alloy ingot was melted each time and melted more than five times to ensure a more uniform composition. The as-cast ingots were spun into ribbons using a single wheel melting-spinning technique (SKY, SD500) in an argon atmosphere at circumferential speeds (S_c) of 21 and 42 m/s, resulting in ribbons with a thickness of 25 μm and a width of 2 mm. Subsequently, the ribbons were annealed in Ar atmosphere for 10 min at temperatures (T_a) of 500, 700 and 850 °C to homogenize the AlNi phase and relieve internal stress.

2.2 Microstructure characterization

The structures of $Al_{50}Ni_{50}$ alloys were analyzed using X-ray diffraction (XRD, Bruker D8 Discover) with Cu K_α radiation (λ=1.54 Å) in the 2θ ranges from 10° to 90°. The fracture morphologies of the as-spun and annealed ribbons were observed using a scanning electron microscope (SEM, JSM−7800F) equipped with an energy-dispersive X-ray spectrometer (EDS). Additionally, transmission electron microscopy (TEM, FEI TALOS F200) was employed to investigate the microstructure of ribbons. The thermodynamic properties of the ribbon

samples were also investigated using differential scanning calorimetry (DSC, NETZSCH−404) at a heating rate of 20 K/min. The lattice constants of AlNi were obtained from the Rietveld analysis method with deduction of the $K_{\alpha 2}$ lines, while the lattice constants (a_0) of AlNi from ribbon precursors were calculated by the extended equation [35]:

$$a_0 = \frac{\lambda}{2\sin\theta}\sqrt{h^2+k^2+l^2} \quad (1)$$

where λ is the radiation wavelength (λ=1.54 Å); θ is the diffraction angle; h, k and l are the crystal plane indices.

2.3 Electrochemical investigation

The electrochemical investigation was conducted using a three-electrode cell with an electrochemical workstation (CHI 660E) at room temperature (25 °C). The ribbons were used as the working electrodes, and their free surfaces were covered with epoxy resin. A saturated calomel electrode (SCE) was served as the reference electrode, while a platinum plate was acted as the counter electrode. The working area was measured after each electrochemical test, which was conducted in 0.6 mol/L NaCl solution. The solution used was prepared with the ultrapure water (electrical resistivity 18.25 MΩ·cm) and high-purity-grade chemicals. An open circuit potential (OCP) test was carried out for 20 min before each electrochemical test. The potential range of the potentiometric dynamic test for the as-spun and annealed ribbons were from −1.1 and −1.2 to 0.8 V, respectively, and the scanning rate was 1 mV/s.

Before the electrochemical impedance spectra (EIS) test, the samples were pretreated at an open circuit potential for 1800 s until the potential fluctuation was less than 5 mV in 10 min. The relevant parameters were obtained by mathematical model, circuit model and corresponding fitting method. The scanning frequency range was set from 0.01 to 100000 Hz, and the amplitude was ±10 mV. To assist in analyzing the variation of corrosion properties of ribbons, we also carried out the immersion experiment in NaCl solution. Specifically, the as-spun and 700 °C annealed ribbons with 21 and 42 m/s of the same initial mass were immersed in 0.6 mol/L NaCl solution and then weighted after drying every 24 h. After the immersion test, the corrosion rates of the four kinds of ribbons can be deduced.

2.4 X-ray photoelectron spectroscopy experiments

The chemical composition of the passive film was analyzed using X-ray photoelectron spectroscopy (XPS, Thermofisher Escalab Xi$^+$, USA) at ambient temperature. The XPS spectra were recorded with Al K_α radiation ($h\nu$=1486.6 eV) from a monochromatic X-ray source and a 400 μm light spot size under a base pressure of 2.0×10^{-7} Pa. The test tube voltage and current were set to be 15 kV and 10 mA, respectively. High resolution spectra were obtained at a pass energy of 30 eV with a step size of 0.05 eV, and the etching rate was 1 nm/s (relative to Ta_2O_5). The XPS spectral analysis was performed using CasaXPS system (Casa Software Ltd, UK). The standard Shirley background subtraction method was used to calibrate the binding energy (E_B). The atomic concentrations of Al, Ni and O were estimated by measuring the peak area of the XPS spectrum divided by the relative atomic sensitivity factor using Casa XPS software.

3 Results and discussion

3.1 Structure

Figure 1 shows the X-ray diffraction patterns of as-spun and annealed $Al_{50}Ni_{50}$ ribbons with 21 and 42 m/s at 500, 700 and 850 °C. Four intense diffraction peaks located at 2θ=30.95, 44.34, 64.49, and 81.60° correspond to (100), (110), (200) and (211) crystal faces, respectively. In addition, there are two tiny peaks at 2θ=55.04° and 73.24° corresponding to (111) and (210) crystal faces, respectively. The as-spun and annealed ribbons are composed of single AlNi phase. As T_a increases, the (100) peak of the ribbons with 21 and 42 m/s changes nonmonotically. To further confirm the variation of crystal orientation, the orientation factor (F) of AlNi (100) surface ($F_{(100)}$) was calculated using the Lotgering equation [36]:

$$F = \frac{P-P_0}{1-P_0},\ P = \frac{\sum I_{(h00)}}{\sum I_{(hkl)}},\ P_0 = \frac{\sum I_{0(h00)}}{\sum I_{0(hkl)}} \quad (2)$$

where $I_{(h00)}$ and $I_{(hkl)}$ are the integral intensities of (h00) and (hkl) diffraction peaks of XRD patterns for experimental samples, respectively, $I_{0(h00)}$ and $I_{0(hkl)}$ are the integral intensities of (h00) and (hkl) diffraction peaks for randomly oriented samples, respectively, P and P_0 are the ratios of integral intensities of (h00) diffraction peaks to those of all

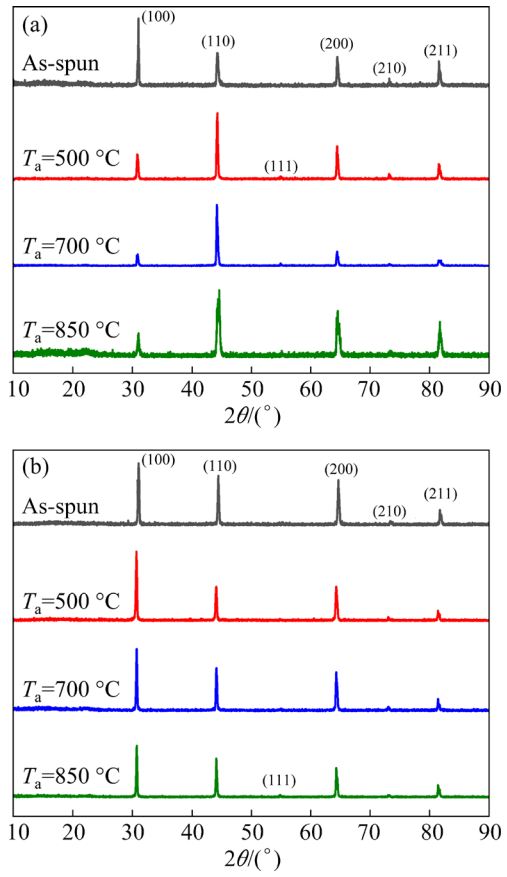

Fig. 1 XRD patterns of as-spun and annealed $Al_{50}Ni_{50}$ ribbons with circumferential speeds of 21 m/s (a) and 42 m/s (b)

(*hkl*) diffraction peaks for the experimental samples and randomly oriented samples, respectively. The preferred orientation factor of (100) face ($F_{(100)}$), position of diffraction peak of AlNi (100) face ($2\theta_{(100)}$), corresponding interplanar spacing ($d_{(100)}$), and lattice parameter a_0 of as-spun and annealed $Al_{50}Ni_{50}$ ribbons are listed in Table 1. And the $F_{(100)}$ and a_0 of as-spun and annealed ribbons are shown in Fig. 2.

As shown in Table 1, the $F_{(100)}$ of $Al_{50}Ni_{50}$ ribbons tends to increase with increasing S_c. As T_a increases, the $F_{(100)}$ of ribbons with 21 m/s first decreases and then increases, dropping to 0.079 from 0.411 and then rising to 0.266. In contrast, the $F_{(100)}$ of ribbons with 42 m/s initially increases to 0.610 from 0.536 and then decreases to 0.492 (Table 1 and Fig. 2(a)). Simultaneously, the a_0 of the ribbons with 21 and 42 m/s increases firstly and then decreases (Table 1 and Fig. 2(b)). According to Refs. [37,38], AlNi has two regions: tension regions with large lattice parameters (a_0 > 2.886 Å) and compression regions with small lattice parameters

Table 1 Preferred orientation factor ($F_{(100)}$) and position ($2\theta_{(100)}$) of AlNi (100) diffraction peak, corresponding interplanar spacing ($d_{(100)}$) and lattice parameter (a_0) of as-spun and annealed $Al_{50}Ni_{50}$ ribbons (The ribbon at 25 °C is as-spun ribbon)

S_c/(m·s^{-1})	T_a/°C	$F_{(100)}$	$2\theta_{(100)}$/(°)	$d_{(100)}$/nm	a_0/Å
21	25	0.411	31.009	0.28816	2.887
	500	0.255	30.851	0.28960	2.891
	700	0.079	30.830	0.28978	2.893
	850	0.266	31.031	0.28796	2.884
42	25	0.536	31.100	0.28733	2.878
	500	0.610	30.731	0.29070	2.897
	700	0.543	30.760	0.29043	2.896
	850	0.492	30.761	0.29043	2.896

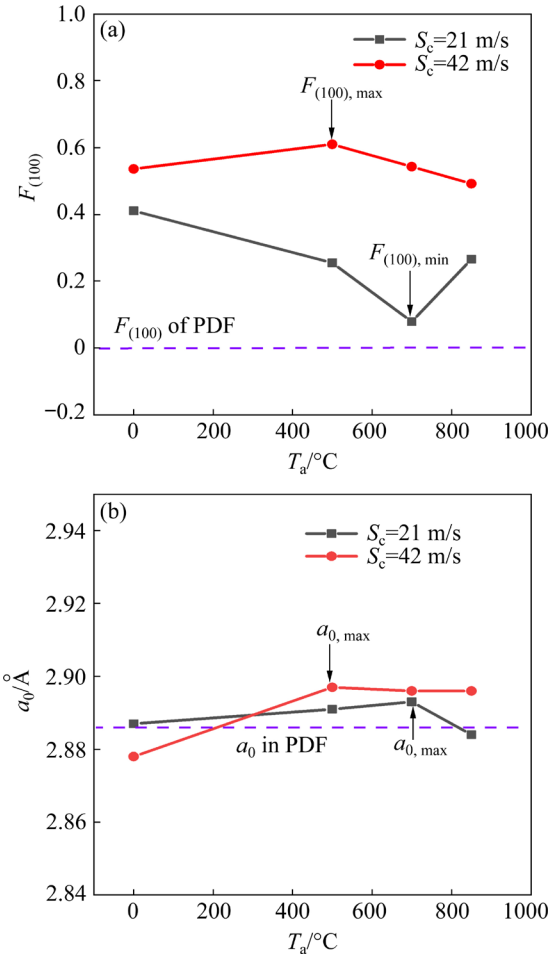

Fig. 2 $F_{(100)}$ (a) and lattice parameter a_0 (b) of as-spun and annealed $Al_{50}Ni_{50}$ ribbons with 21 and 42 m/s

(a_0 < 2.886 Å); the tensile stress can be neutralized by the compressive stress induced by oxidation, and the annealed ribbons with 42 m/s have fewer total stress defect than the counterparts with 21 m/s. With increasing T_a, the maximum a_0 of ribbons with

42 m/s appears at 500 °C, earlier than that of ribbons with 21 m/s at 700 °C. This indicates that some lattice defects, such as vacancies, dislocations, and grain boundaries, disappear more quickly in ribbons with 42 m/s.

Figure 3 shows the SEM images of fracture surfaces of $Al_{50}Ni_{50}$ ribbons after tensile breaking, and the average grain sizes are listed in Table 2. In the case of 21 m/s, the as-spun ribbon exhibits an intergranular fracture surface throughout the cross-section, with the grain boundaries perpendicular to the surface (roller/air side), indicating grain growth against the direction of heat flow (Fig. 3(a)); at T_a=500 °C or higher, the grain size of ribbon

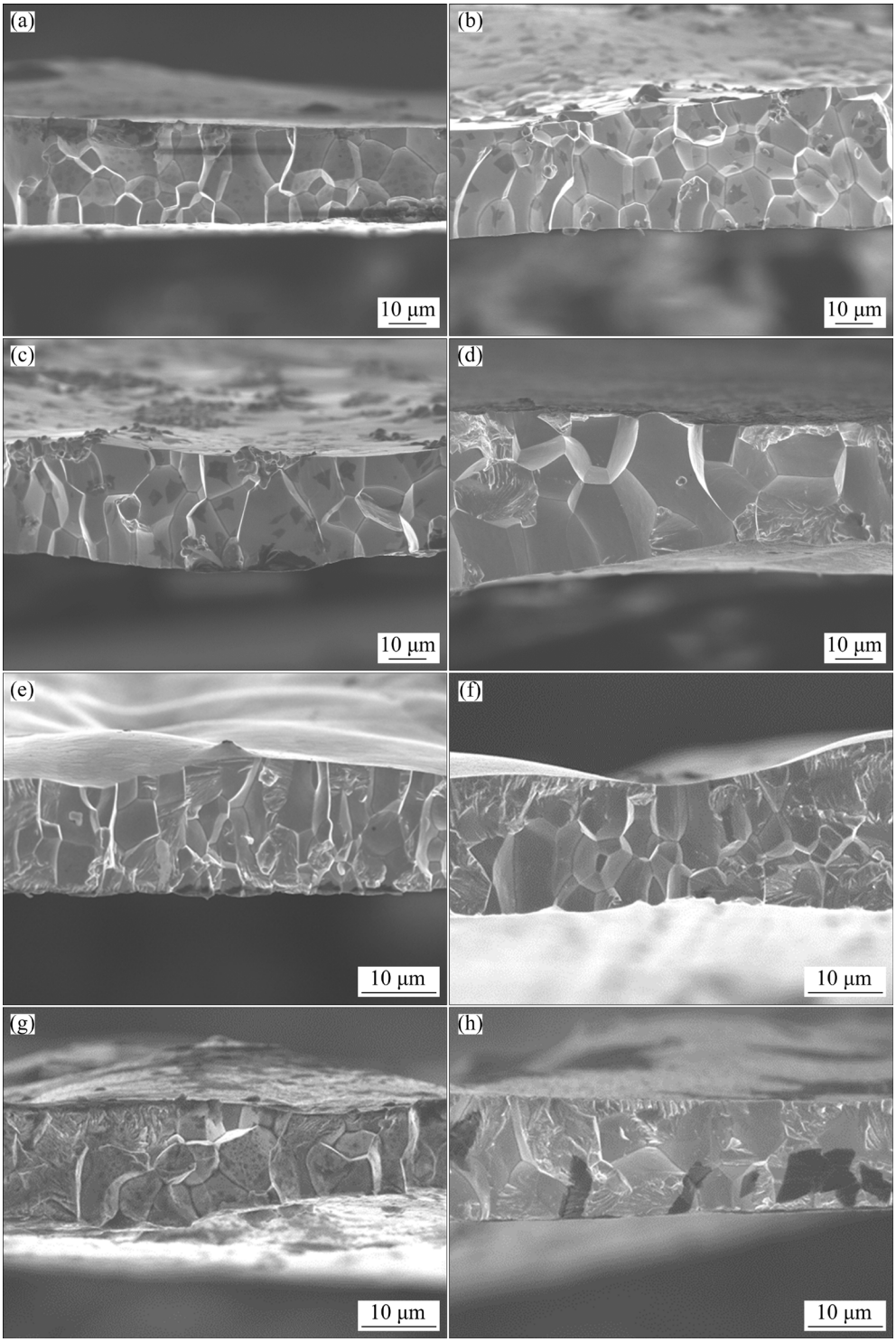

Fig. 3 SEM images of fracture surfaces of as-spun and annealed $Al_{50}Ni_{50}$ ribbons after tensile breaking with 21 m/s (a−d) and 42 m/s (e−h) at different temperatures: (a, e) 25 °C; (b, f) 500 °C; (c, g) 700 °C; (d, h) 850 °C

Table 2 Grain size of fracture surfaces of present ribbons calculated by Nanomeasure software

S_c/(m·s^{-1})	Grain size/μm			
	25 °C	500 °C	700 °C	850 °C
21	9.30	11.64	14.54	17.40
42	6.44	7.61	8.85	9.86

increases and the fracture remains intergranular, with some grain edges displaying transgranular fracture (Figs. 3(b−d) and Table 2). In the case of 42 m/s, the grain boundaries beneath the surface of the as-spun ribbon are perpendicular to the surface, and the transgranular fracture area is higher than that of the as-spun ribbon with 21 m/s (Fig. 3(e)). With increasing T_a, the grain size of ribbon and transgranular fracture area tend to increase, and the grain boundaries tend to deviate from the perpendicular direction of surface (Figs. 3(f−h) and Table 2).

These findings confirm the occurrence of nucleation and growth of recrystallization within the AlNi ribbons during the annealing process. With the increase of cooling rate, the nucleation rate of the solid phase increases while its growth rate slows down [39,40]. It is expected that the ribbons with S_c=42 m/s would have a smaller grain size than that with S_c=21 m/s, providing them with more opportunities to grow in their preferred orientation and resulting in a higher $F_{(100)}$ factor (Fig. 2(a)).

To further characterize the microstructure of the $Al_{50}Ni_{50}$ ribbons, we conducted TEM investigations on both the as-spun and 700 °C annealed ribbons with 21 and 42 m/s, as shown in Fig. 4. The as-spun ribbon with 21 m/s exhibits numerous dislocation lines in random directions (Fig. 4(a)), and its corresponding SAED pattern can be singly identified as AlNi phase with $d_{(100)}$= 2.883 Å (Fig. 4(b)). In the high resolution TEM, the matrix zone and its Fast Fourier transformation (FFT) pattern confirm AlNi phase with $d_{(100)}$= 2.973 Å, which is higher than the value from the SAED pattern (Figs. 4(c, d)); a pentagonal precipitate (a square with a truncated corner) has a similar FFT pattern to matrix, with front surfaces of (100) and (110) directions (Figs. 4(c, e)), the $d_{(100)}$ of the precipitate is 2.929 Å, which is lower than that of the matrix (Fig. 4(e)). The precipitate is an earlier crystalline nuclei and trapped by the later solidified phase [40−42].

The ribbon annealed at 700 °C with S_c=21 m/s also exhibits numerous dislocation lines in an ordered net-like shape (Fig. 4(f)); and the $d_{(100)}$ of its SAED pattern for sole AlNi phase is 2.873 Å (Fig. 4(g)). In the high resolution TEM, the matrix zone is also identified as sole AlNi phase with $d_{(100)}$=2.968 Å, which is higher than the value from the SAED pattern (Figs. 4(h, i)); a pentagonal precipitate is identified as AlNi phase with the front surface of (110) direction for the long sides, and its $d_{(100)}$ is 2.899 Å, which is lower than the matrix (Figs. 4(h, j)). This is consistent with the recrystallization phenomenon observed in Al- and Fe-based alloys [28,43,44].

The as-spun ribbon with 42 m/s contains fewer dislocation lines, including helical dislocations, compared with the ribbons with 21 m/s (Fig. 4(k)). The $d_{(100)}$ of its SAED for sole AlNi phase is 2.873 Å (Fig. 4(l)). In the high resolution TEM, the AlNi matrix zone has a higher $d_{(100)}$ (3.012 Å) than the value from the SAED pattern (Figs. 4(m, n)); the $d_{(100)}$ of the octagonal AlNi precipitate with front surfaces of (100) and $(1\bar{1}0)$ directions is 2.987 Å, which is lower than the matrix (Figs. 4(m, o)). The ribbon annealed at 700 °C with 42 m/s has minimal dislocation lines and many dark dots (Fig. 4(p)); its corresponding SAED pattern can be singly identified as AlNi phase with $d_{(100)}$=2.894 Å (Fig. 4(q)); the high resolution TEM shows the matrix of AlNi phase and the octagonal AlNi precipitate with front surfaces of (100) and $(1\bar{1}0)$ directions (Figs. 4(q−s)). The $d_{(100)}$ of the precipitate (2.872 Å) is also lower than the martix (3.081 Å). Here, the ribbon annealed at 700 °C with 42 m/s has fewer dislocation and stress defects than other ribbons.

It should be noted that the phases identified by TEM only reflect the local microstructure of the samples. The brightest SAED spots denote the (110) plane AlNi (Figs. 4(b), (g), (l) and (q)), corresponding to the peak at 2θ=44° in the XRD patterns (Fig. 1). From the fast Fourier transform (FFT) of the high-resolution image (Figs. 4(c), (h), (m) and (r)), the $d_{(100)}$ value of the matrix (District 1) is always greater than that of its adjacent precipitate (District 2) and further away the standard value (2.88 Å), indicating that the precipitate is closer to the defect-less and perfect AlNi phase than the matrix. Furthermore, with increasing S_c, the precipitate shape changes from a truncated square

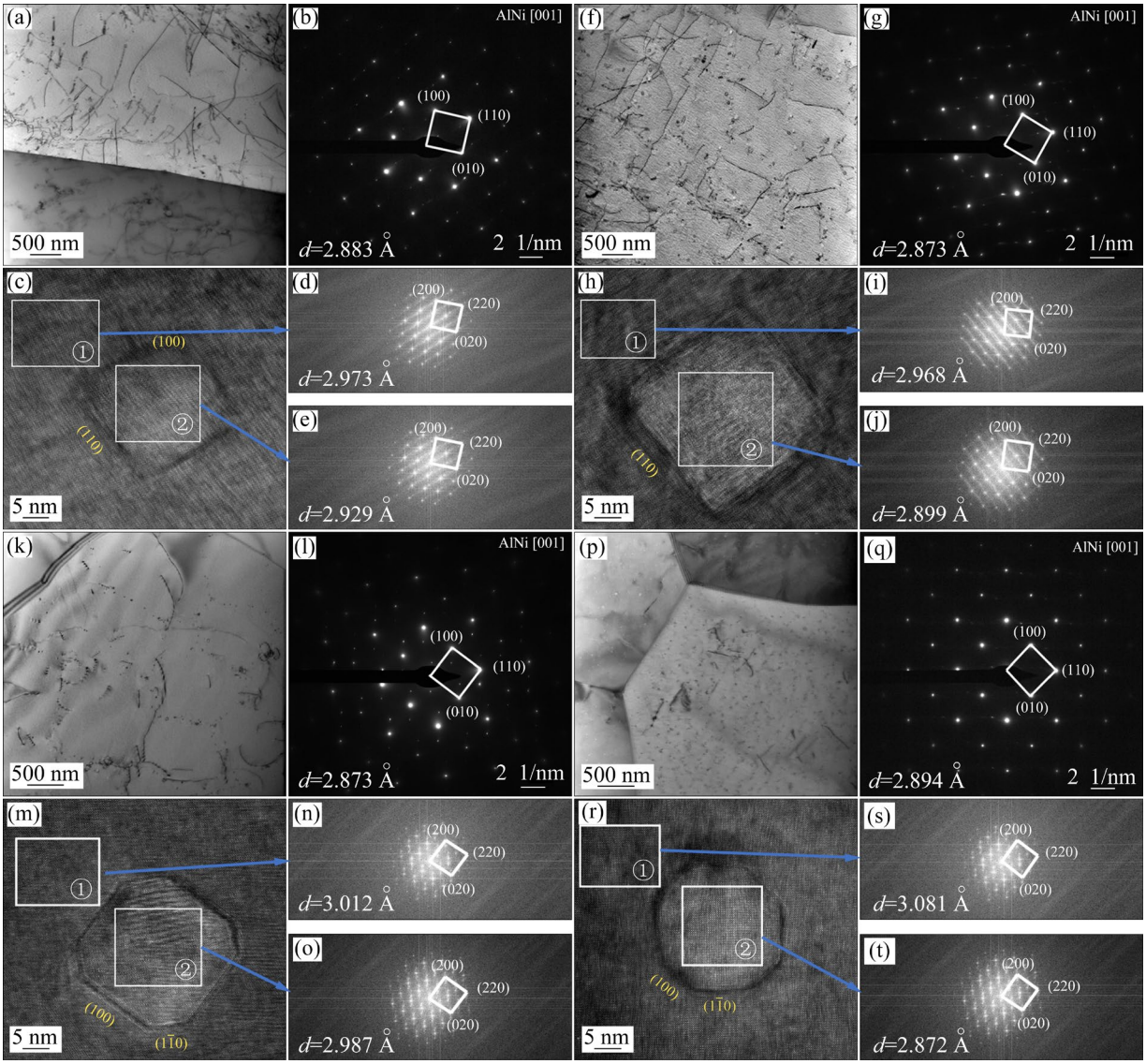

Fig. 4 Low resolution TEM images, corresponding selected area electron diffraction (SAED) patterns, high resolution TEM images and fast Fourier transformation (FFT) patterns of as-spun and annealed $Al_{50}Ni_{50}$ ribbons: (a−e) S_c=21 m/s, T_a=25 °C; (f−j) S_c=21 m/s, T_a=700 °C; (k−o) S_c=42 m/s, T_a=25 °C; (p−t) S_c=42 m/s, T_a=700 °C (The distance d of (100) face is deduced from the corresponding diffraction patterns)

to an octagon with more (100) surfaces, which is reinforced after annealing and consistent with the variation tendency of the orientation factor $F_{(100)}$ (Figs. 2(a) and 4(r)).

To check the recrystallization behavior during the heating process, two consecutive runs of DSC analysis were conducted on as-spun and annealed $Al_{50}Ni_{50}$ ribbons with the same heating rate of 20 K/min, as shown in Fig. 5. Here, the peak of first DSC curve under the 2nd curve (considered as base line) is labeled as exothermic peak (ΔH_{ex}), and the peak beyond the 2nd DSC curve is labeled as endothermic peak (ΔH_{en}). According to Ref. [45], the exothermic peak in the measured thermograms corresponds to the stored energy released by the recrystallization process.

For the as-spun ribbon with 21 m/s, two endothermic peaks were observed at approximately 400 and 800 °C, along with an exothermic peak at around 600 °C. The ribbon annealed at 500 °C showed similar peaks. However, the endothermic peak at 400 °C disappeared in the ribbons with $T_a \geq$ 700 °C, and the ribbon annealed at 850 °C showed no exothermic peak (Fig. 5(a)), indicating that, as T_a is high enough, the endothermic heat for defect extinction and the barrier to recrystallization may

decrease. Hence, it is understood that the recrystallization starting temperature of 700 °C annealed ribbon with 21 m/s is lower than that of as-spun and 500 °C annealed ribbons. Subsequently, grain growth occurred and absorbed heat, which was confirmed by the endothermic peaks at around 800 °C (Fig. 5(a)).

For the ribbons with 42 m/s, there are no noticeable endothermic peaks before the recrystallization process, indicating that with increasing S_c, the barrier to recrystallizing decreases, similar to increasing T_a. At around 600 °C, both the as-spun and annealed ribbons with 42 m/s exhibit an exothermic peak corresponding to recrystallization (Fig. 5(b)). At around 900 °C, there are endothermic peaks associated with grain growth after recrystallization. The recrystallization process is more easily triggered in ribbons with 42 m/s, which is consistent with a higher $F_{(100)}$ value compared to ribbons with 21 m/s (Fig. 2(a)).

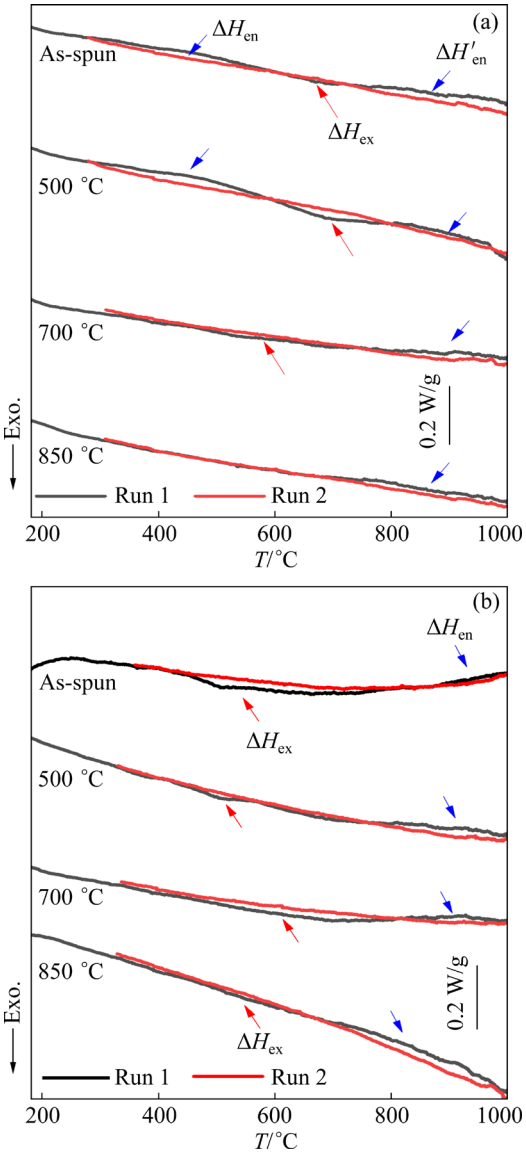

Fig. 5 DSC thermograms for two consecutive runs at heating rate of 20 K/min of as-spun and annealed $Al_{50}Ni_{50}$ ribbons with 21 m/s (a) and 42 m/s (b) (Run 2 curves are considered as the base lines for the corresponding Run 1 curves)

3.2 Electrochemical analysis

Figure 6 shows potentiodynamic polarization plots of as-spun and annealed $Al_{50}Ni_{50}$ ribbons in neutral NaCl solution. The corrosion potential φ_{corr}, corrosion current density J_{corr}, pitting potential φ_{pit} and passive range $\varphi_{pit}-\varphi_{corr}$ are summarized in Table 3. Here, the anodic polarization curves of eight ribbons show an obvious passive platform without a clear anodic Tafel region, thus the cathodic branches are used to approximate their J_{corr}. The passive platforms of both the as-spun and annealed ribbons with 21 m/s are relatively short, and their passive current densities J_{pass} are scattered.

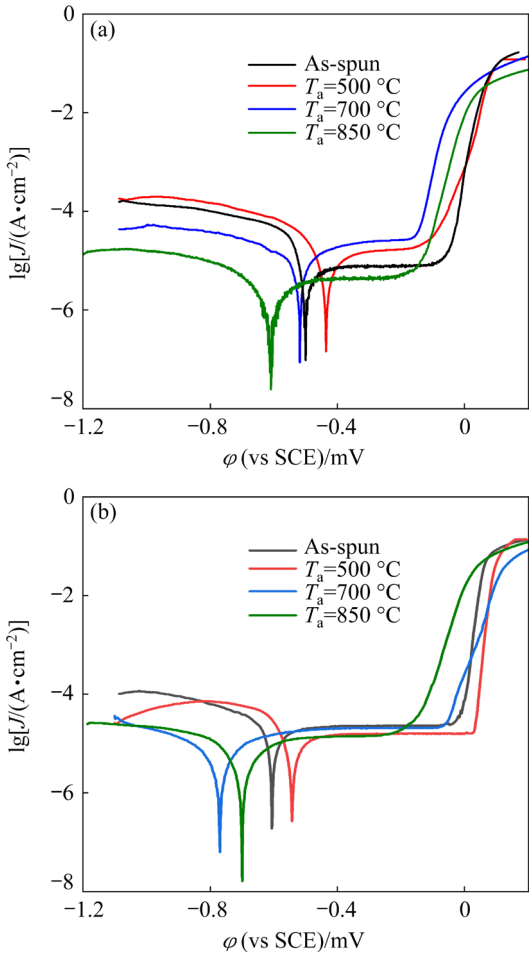

Fig. 6 Potentiodynamic polarization plots of as-spun and annealed $Al_{50}Ni_{50}$ ribbons with 21 m/s (a) and 42 m/s (b) in neutral solutions

Table 3 Parameters deduced from potentiodynamic polarization plots in Fig. 6 like corrosion potential φ_{corr}, corrosion current density J_{corr}, pitting potential φ_{pit} and passive range $\varphi_{pit}-\varphi_{corr}$ with standard deviation from 0.05 to 1.30 (The ribbon with 25 °C is as-spun ribbon)

S_c/(m·s^{-1})	T_a/°C	φ_{corr}(vs SCE)/V	J_{corr}/(μA·cm^{-2})	φ_{pit}(vs SCE)/V	($\varphi_{pit}-\varphi_{corr}$) (vs SCE)/V
21	25	−0.50	4.8	−0.05	0.45
	500	−0.43	22.6	−0.11	0.32
	700	−0.51	13.7	−0.15	0.36
	850	−0.62	3.1	−0.14	0.48
42	25	−0.60	31.2	−0.03	0.57
	500	−0.58	34.4	0.01	0.59
	700	−0.76	9.2	−0.06	0.70
	850	−0.69	11.4	−0.20	0.49

Additionally, the 700 °C annealed ribbon with 21 m/s exhibits the highest J_{corr}. The higher the corrosion current density is, the less resistant to corrosion the material is, indicating that the passive film of the ribbon is possibly loose and porous (Fig. 6(a)). In contrast, the J_{pass} values of ribbons with 42 m/s almost coincide (Fig. 6(b)).

With increasing T_a, the pitting potential (φ_{pit}) of ribbons with 21 m/s decreases to −0.15 V at 700 °C and then increases to −0.14 V at 850 °C. In contrast, the φ_{pit} of ribbons with 42 m/s increases to 0.01 V at 500 °C, and then decreases to −0.2 V at 850 °C. Overall, the changing tendency of the pitting potential (φ_{pit}) is consistent with the orientation factor $F_{(100)}$ (Fig. 2(a)). In conclusion, ribbons with a higher $F_{(100)}$ exhibit a better corrosion resistance, which is consistent with Refs. [32−34].

Figure 7 shows the measured and fitted Nyquist plots of as-spun and annealed $Al_{50}Ni_{50}$ ribbons in neutral NaCl solution. Among several candidate equivalent circuits, the equivalent circuit $R(Q(R(QR)))$ is suitable for fitting the measured EIS data, with a chi-square value of less than 10^{-3}. The non-ideal capacitance behavior caused by local inhomogeneity is represented by the constant phase element CPE (Q), whose impedance is defined as [46−48]

$$Q=(j\omega)^{-n}/Y_0 \quad (3)$$

where j is the imaginary number, ω is the angular frequency (rad·s^{-1}), the factor n, defined as a CPE power, is adjustable parameter that always lies between 0.5 and 1, and Y_0 is the frequency independent parameter (s^n·Ω^{-1}·cm^{-2}). When n=0.5, Q reflects a Warburg impedance with diffusion character. For 0.5<n<1, Q represents a distribution of dielectric relaxation time in the frequency domain, and for n=1, Q describes a pure capacitor. The fitting results of EIS tests of eight ribbons are summarized in Table 4.

The Nyquist semicircle diameter of $Al_{50}Ni_{50}$ ribbons with S_c=21 m/s in neutral solution decreases significantly after annealing at 700 °C (Fig. 7(a)). On the contrary, the Nyquist semicircle diameter of ribbons with S_c=42 m/s increases after annealing at 700 °C (Fig. 7(b)). Furthermore, the reaction and

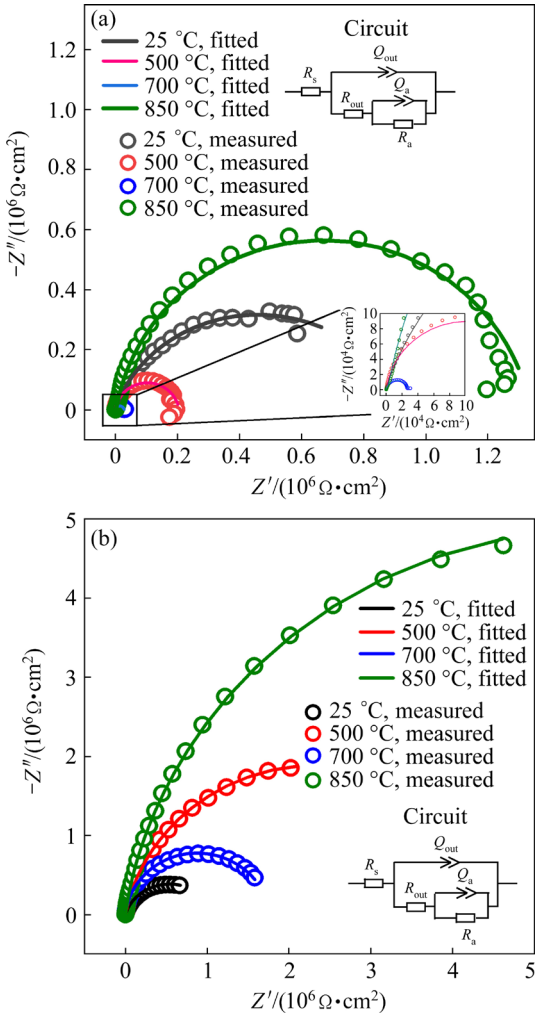

Fig. 7 Nyquist plots of as-spun and annealed $Al_{50}Ni_{50}$ ribbons in neutral solution with S_c=21 m/s (a) and S_c=42 m/s (b) (Symbols show the experimental data while solid lines are fitting results. The upper inset in (a) and lower inset in (b) denote the general fitted circuits; and the lower inset in (a) denotes the magnification of the EIS curves ($\chi^2 \le 0.001$))

total resistances (R_a and R_{total}) of the ribbons with 21 and 42 m/s change similarly to their Nyquist semicircle diameters (Table 4) and are consistent with their orientation factor $F_{(100)}$ (Fig. 2(a)). In summary, the EIS results are in agreement with the orientation factor $F_{(100)}$ and Tafel results.

Figure 8 shows the Bode plots of the as-spun and annealed $Al_{50}Ni_{50}$ ribbons in the neutral NaCl solution. Bode plots are roughly divided into three regions [49−51]: (1) low frequency f interval (10^{-2}−10^{0} Hz) is mainly reflected by the resistance (R_a) and capacitance (Q_a) of the electrochemical reaction at the interface between the ribbon and passive film; (2) intermediate frequency area (10^{0}−10^{3} Hz) is mainly reflected by the resistance (R_{in}) and capacitance (Q_{in}) of the inner passive film; (3) high frequency region (10^{3}−10^{5} Hz) is mainly reflected by the resistance (R_{out}) and (Q_{out}) of the outer passive film or corrosion products. In the low f range, the total impedance $|Z|$ of the measured ribbons is consistent with their Nyquist semicircle diameters (Fig. 7).

For the ribbons with 21 m/s, in the low f range (10^{-2}−1 Hz), the phase angle curve of the as-spun ribbon has a small peak P_1, while the annealed counterparts do not have it. In the f range of 1−10^{4} Hz, the phase angle curve of the as-spun ribbon has a kink including two overlapped peaks P_2 and P_3, while 700 °C annealed counterpart has a single peak P_1. In the high f range (>10^{4} Hz), 850 °C annealed ribbon has a phase angle rise surpassing 90° while other counterparts do not (Fig. 8(a)). For the ribbons with 42 m/s, in the low f range (10^{-2}−1 Hz), the phase angle curves of four ribbons have no peak. In the f range of 1−10^{4} Hz, the phase angle curves of the as-spun and 700 °C annealed ribbons both have two peaks: P_1 and P_2. In the high f range (>10^{4} Hz), the phase angle curves of the three annealed ribbons have a drastic rise, indicating that an outer film or corrosion products are formed (Fig. 8(b)). In addition, the peaks at high frequency are valuable to further study.

Table 4 Fitting parameters from EIS measurements (R_s solution resistance, constant phase element CPE and out layer resistance (Q_{out} and R_{out}), CPE and reaction resistance (Q_a and R_a), total resistance (R_{total}) and total impedance ($|Z|$))

S_c ($m\cdot s^{-1}$)	T_a/ °C	R_s/ ($\Omega\cdot cm^2$)	Y_0 of Q_{out}/ ($10^{-6}s^n\cdot\Omega^{-1}\cdot cm^{-2}$)	n of Q_{out}	R_{out}/ ($10^6\,\Omega\cdot cm^2$)	Y_0 of Q_a/ ($10^{-5}s^n\cdot\Omega^{-1}\cdot cm^{-2}$)	n of Q_a	R_a/ ($10^5\,\Omega\cdot cm^2$)	R_{total}/ ($10^5\,\Omega\cdot cm^2$)	$\|Z\|$/ ($10^6\,\Omega\cdot cm^2$)
21	25	0.38	4.58	0.88	0.42	2.28	1	3.0	7.2	0.62
	500	1.60	7.53	0.91	0.40	4.19	0.80	0.8	4.8	0.18
	700	1.25	0.96	1	0.05	0.18	0.72	0.1	0.7	0.05
	850	1.26	1.48	0.85	0.60	0.25	0.35	3.5	9.5	1.40
42	25	1.80	3.26	0.90	1.07	0.20	0.35	3.8	14.5	0.73
	500	0.14	1.41	0.92	3.56	0.14	1	41.5	77.0	2.80
	700	0.99	1.85	0.96	1.65	1.42	0.80	9.0	25.5	1.60
	850	2.19	0.27	0.99	0.20	0.01	0.99	8.9	10.9	9.30

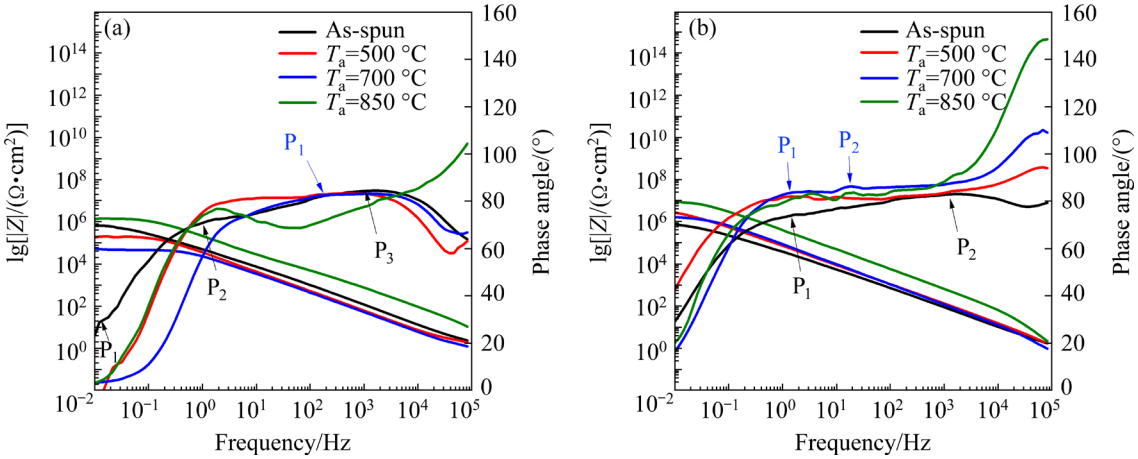

Fig. 8 Bode plots of as-spun and annealed $Al_{50}Ni_{50}$ ribbons in neutral solution with 21 m/s (a) and 42 m/s (b)

In the Bode plot, a phase angle closer to 90° indicates a more dense and stable passive film on the corroded surface [52]. Accordingly, the passive film of the as-spun ribbon with 21 m/s is more stable and compact than that of the 700 °C annealed counterpart, and the passive film of the 700 °C annealed ribbon with 42 m/s is more stable and compact than that of the as-spun counterpart. Moreover, ribbons with a phase angle rise at high f exhibit large total resistance (R_{total}) and impedance $|Z|$ (Table 4), indicating that the as-spun and 700 °C annealed ribbons with 42 m/s possess higher corrosion resistance than the counterparts with 21 m/s and being consistent with the measured passive range in Fig. 6 and Table 3. Immersion experiments were also conducted, and the corrosion rates of the as-spun and 700 °C annealed ribbons with 21 m/s were found to be 0.046 and 0.226 mm/a, respectively; while those of the as-spun and 700 °C annealed ribbons with S_c=42 m/s were 0.017 and 0.010 mm/a, respectively. The results of the immersion test confirm the electrochemical testing results.

3.3 Etching XPS analysis

The etching XPS analysis results of as-spun and annealed $Al_{50}Ni_{50}$ ribbons with 21 m/s are shown in Fig. 9. In the case of as-spun ribbon, with increasing etching time t_e, the Al 2p peak at high binding energy (E_B) shifts left and then right with a large shifting scope, while the peak area at low E_B tends to increase with a constant position (Fig. 9(a)). The Ni 2p peak area at high E_B is low and that at low E_B tends to increase with t_e (Fig. 9(b)); the O 1s

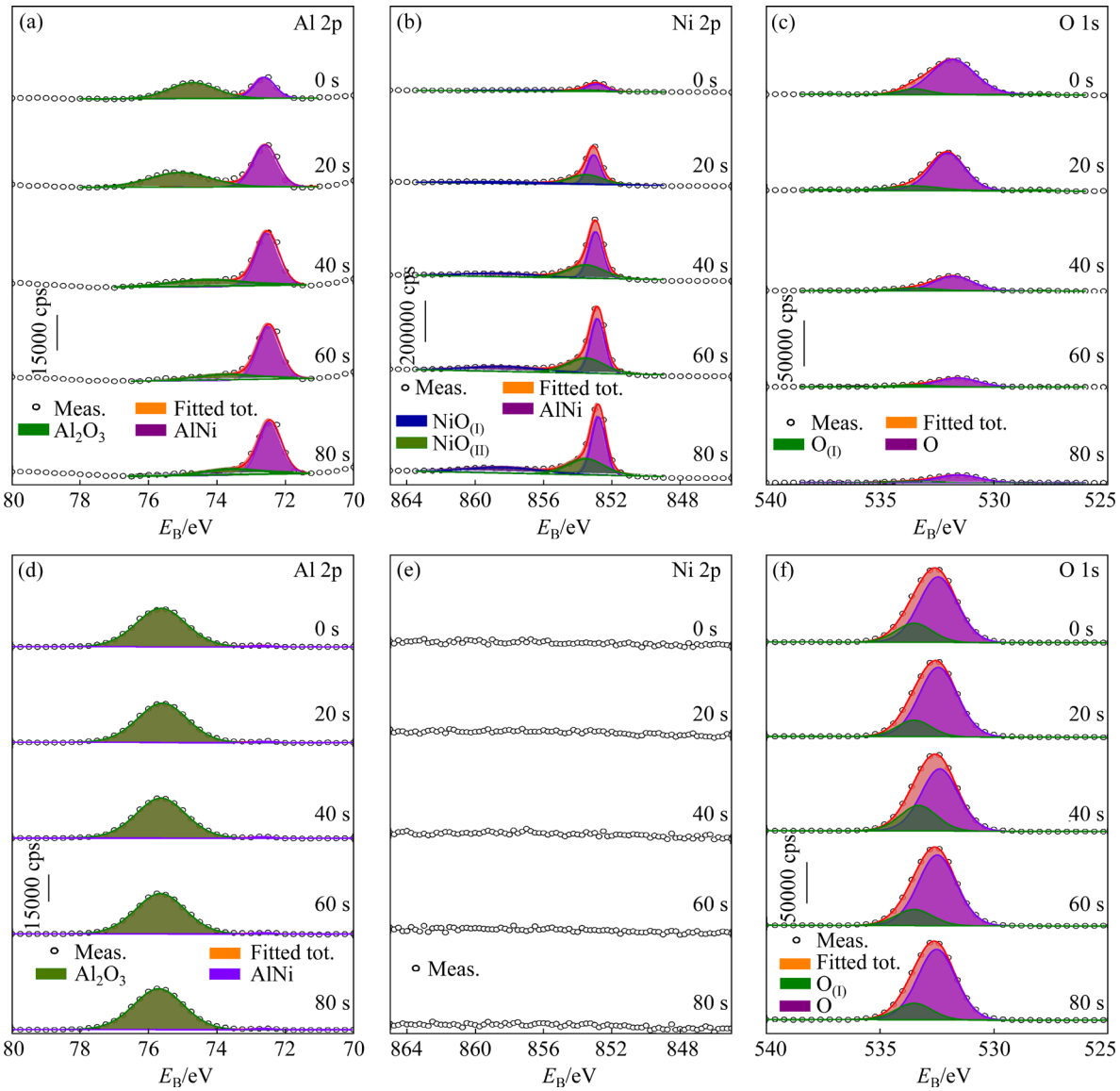

Fig. 9 Al 2p, Ni 2p and O 1s XPS spectra of as-spun (a−c) and 700 °C annealed (d−f) $Al_{50}Ni_{50}$ ribbons with S_c=21 m/s

spectra can be decomposed into two peaks and their total area tends to decrease with increasing time, which is opposite to the trend observed for Ni 2p (Fig. 9(c)). In the case of 700 °C annealed ribbon, with increasing t_e, the Al 2p peak at high E_B remains nearly constant and at a fixed position, and the peak at low E_B is very low (Fig. 9(d)). The Ni 2p peak disappears after annealing (Fig. 9(e)). The O 1s spectra have a constant area with increasing t_e, which can be decomposed into two peaks (Fig. 9(f)). Here, Al 2p peaks at 74.7 and 72.6 eV correspond to Al_2O_3 and AlNi, respectively. In the Al 2p spectra of as-spun ribbon (Fig. 9(a)), the AlNi peak increases to the upper limit and the Al_2O_3 peak decreases to a bottom limit as t_e is enough, indicating that the testing point is approaching to the AlNi matrix.

The etching XPS analyses of the as-spun and 700 °C annealed $Al_{50}Ni_{50}$ ribbons with 42 m/s are shown in Fig. 10. In the case of as-spun ribbon, the Al 2p peak positions have the same change tendence as those with 21 m/s. In addition, with increasing t_e, the Al 2p peak area at high E_B tends to increase and then decrease in a slighter degree than the counterpart with 21 m/s, indicating that the as-spun ribbon has a thicker Al_2O_3 passive film than the latter (Fig. 10(a)). The Ni 2p peak area at high E_B is low and that at low E_B tends to increase with t_e (Fig. 10(b)). The O 1s spectra can be decomposed into two peaks and their total area tends to increase first and then decrease with increasing t_e (Fig. 10(c)). In the case of 700 °C annealed ribbon, with increasing t_e, the Al 2p peak at high E_B tends to increase and then decrease with a small position

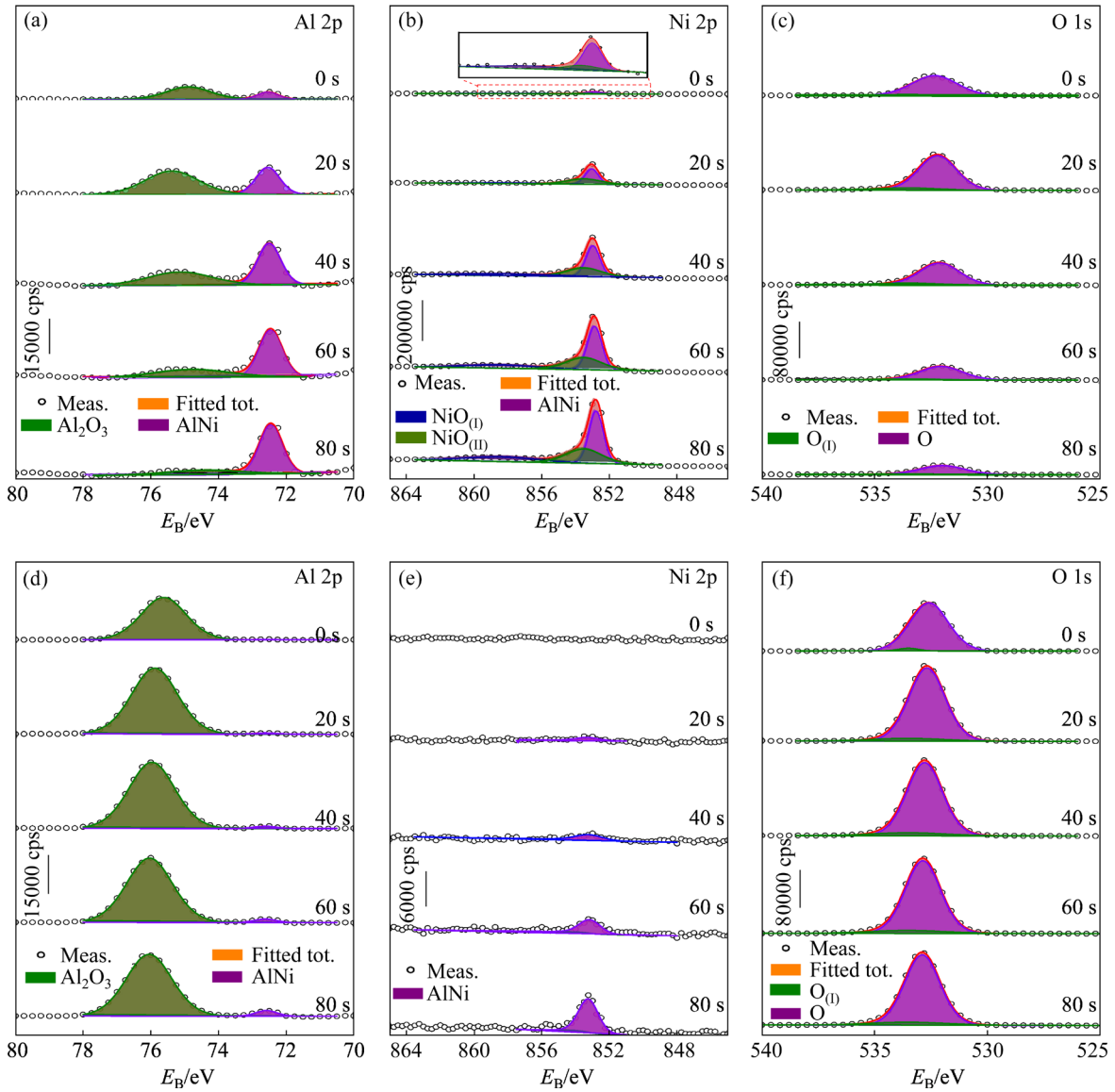

Fig. 10 Al 2p, Ni 2p and O 1s XPS spectra of as-spun (a−c) and 700 °C annealed (d−f) $Al_{50}Ni_{50}$ ribbons with S_c=42 m/s

fluctuation, and the small peak at low E_B tends to increase with a constant position (Fig. 10(d)). The Ni 2p peak at high E_B still disappears and that at low E_B tends to increase with t_e (Fig. 10(e)). The O 1s spectra can also be decomposed into two peaks and their total area increases first and then decreases with increasing t_e (Fig. 10(f)).

Figure 11 shows the t_e-dependent XPS peak positions of ribbons with 21 and 42 m/s. With increasing t_e from 0 to 20 s, the high E_B of Al_2O_3 peak increases drastically and its variation behavior with 21 m/s changes as t_e increases from 40 to 60 s. Thus, the Al_2O_3 peak position of the as-spun ribbon with 21 and 42 m/s can be divided into three and two regions, respectively, and Region II with 21 m/s has a steep slope than 42 m/s (Fig. 11(a)). After annealing at 700 °C, the Al_2O_3 peak position of the ribbon with 42 m/s can be divided into two regions, and the ribbon with 21 m/s has only one region (Fig. 11(b)).

The Ni 2p peak position at high E_B of as-spun ribbons with 21 and 42 m/s has a similar variation with their Al 2p peaks (Fig. 11(c)). However, after annealing at 700 °C, the Ni 2p peaks at two E_B of

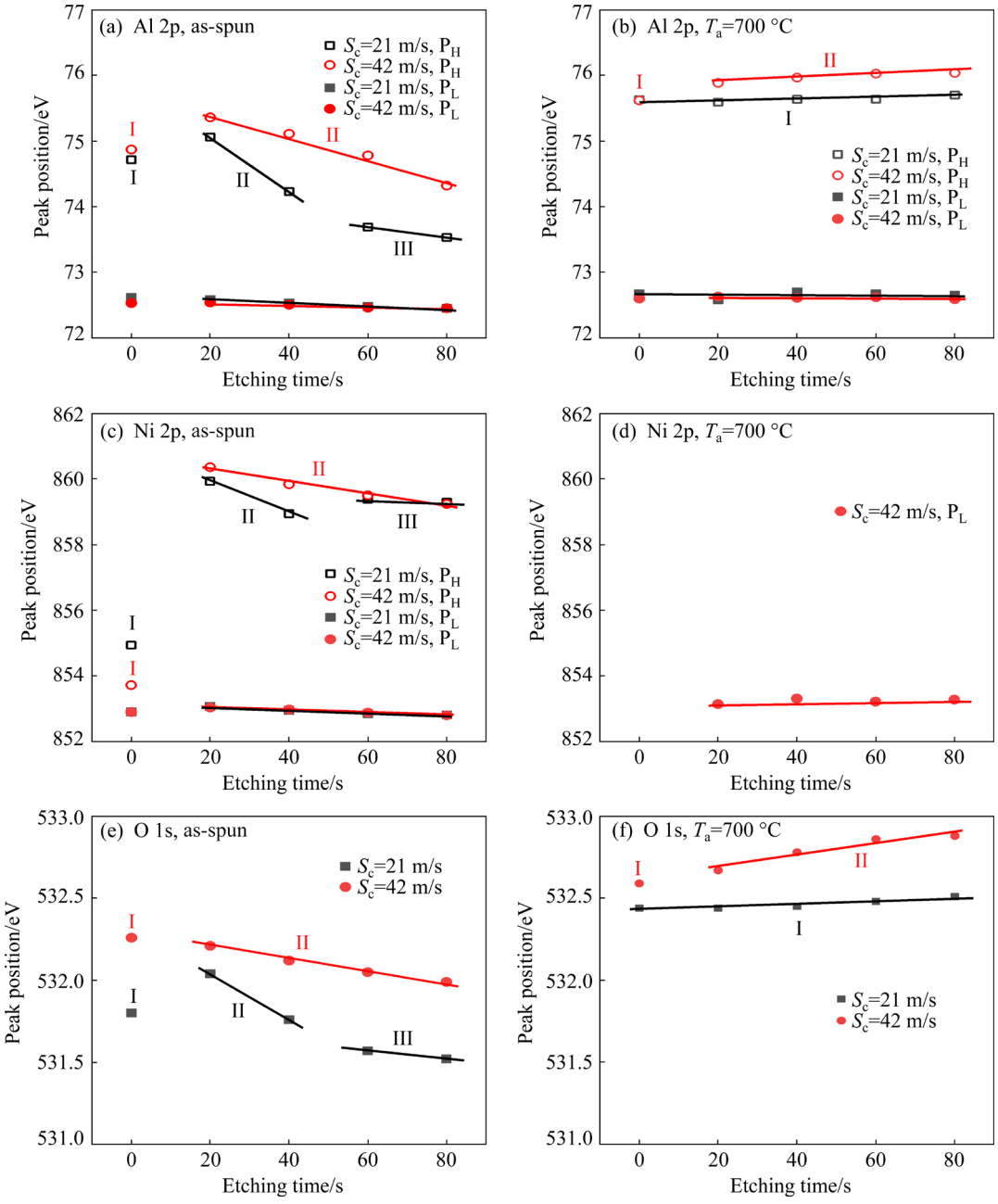

Fig. 11 Etching time (t_e) dependent XPS peak positions of $Al_{50}Ni_{50}$ as-spun and 700 °C annealed ribbons with 21 and 42 m/s: (a) As-spun, Al 2p; (b) Annealed state, Al 2p; (c) As-spun, Ni 2p; (d) Annealed state, Ni 2p; (e) As-spun O 1s; (f) Annealed state, O 1s (Symbols show the experimental data while solid lines are fitting data)

the ribbon with 21 m/s disappeared, and the ribbon with 42 m/s has only low E_B peak as $t_e > 0$ (Fig. 11(d)). The O 1s peak positions of the as-spun ribbon with 21 and 42 m/s can be divided into three and two regions, respectively, corresponding to Al 2p peak positions (Fig. 11(e)). After annealing at 700 °C, the O 1s peak positions of the ribbon with 42 m/s can be divided into two regions, but the ribbon with 21 m/s has one region (Fig. 11(f)).

Combining the results above, the passive film structures of the as-spun and annealed $Al_{50}Ni_{50}$ ribbons with two different S_c values can be schematically illustrated in Fig. 12. The measured film of as-spun AlNi samples with 21 m/s has three oxide layers: the outer layer with abundant Al_2O_3 + AlNi + slight NiO, the middle layer with abundant Al_2O_3 + AlNi + slight NiO, and the inner layer with abundant AlNi + slight Al_2O_3 + slight NiO (Fig. 12(a)). The oxides in Region III like Al_2O_3 and NiO were possibly formed by the AlNi matrix during the etching process, which can be reflected by P_1 in the phase angle curve (Fig. 8(a)). The as-spun AlNi samples with 42 m/s has two oxide layers: the outer layer with abundant Al_2O_3 + slight AlNi + slight NiO, and the inner layer with Al_2O_3 + abundant AlNi + slight NiO (Fig. 12(b)). The passive oxide film of samples with 42 m/s was found to be thicker than that of samples with 21 m/s (Figs. 9−11). After annealing at 700 °C, the etching XPS analysis revealed that the passive film of the ribbon with 21 m/s comprised a sole Al_2O_3 oxide layer (Fig. 12(c)), while the ribbon with 42 m/s has two oxide layers: the outer layer with sole Al_2O_3 and the inner layer with abundant Al_2O_3 + slight AlNi (Fig. 12(d)). These layers were reflected in the corresponding phase angle curves (Fig. 8).

The binding energy of Al 2p and O1s in Region I of the 700 °C annealed ribbon with 42 m/s is lower than that in Region II (Figs. 11(b) and (f)); meanwhile, the Ni 2p peak of 700 °C annealed

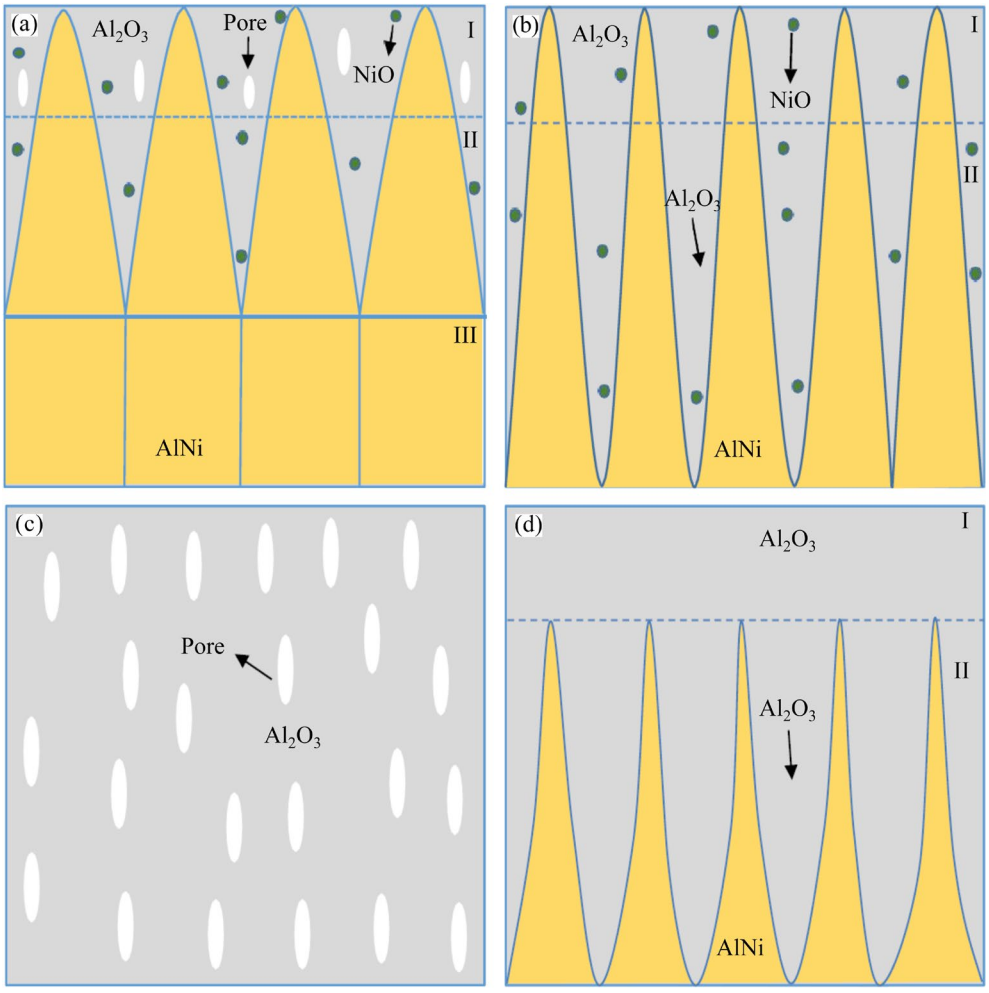

Fig. 12 Schematic illustration of passive film structures of as-spun and 700 °C annealed $Al_{50}Ni_{50}$ ribbons: (a) S_c=21 m/s, as-spun; (b) S_c=21 m/s, T_a=700 °C; (c) S_c=42 m/s, as-spun; (d) S_c=42 m/s, T_a=700 °C

ribbon with 21 m/s disappears (Fig. 9(e)). Combining the polarization test (Figs. 6−8 and Table 3), it is evident that the Al_2O_3 film of the 700 °C annealed ribbon with 21 m/s in Region I is loose with porous, while the as-spun and 700 °C annealed ribbons with 42 m/s have a thinner Al_2O_3 film in Region I and a thicker and more intact inner layer (Al_2O_3 + AlNi) in Region II. These observations suggest that finer grains resulting from the increase in S_c (Fig. 3) provide more opportunities for oxygen atoms to enter the grains.

The fine grains also bring about some other changes in the microstructure of the AlNi phase, such as internal stress, texture and recrystallization (Figs. 2−5). Here, the as-spun and annealed ribbons with 42 m/s have a higher orientation factor $F_{(100)}$ than that of ribbons with 21 m/s (Fig. 2(a)). It is known that the Al (100) face of the single Al crystal has a higher corrosion resistance than its Al (110) face [32−34]. Therefore, it can be inferred that the corrosion resistance of AlNi ribbon can be improved by increasing S_c and additional annealing. These findings provide a new strategy for enhancing the corrosion resistance of Al-based alloys.

4 Conclusions

(1) The as-spun and annealed ribbons with circumferential speeds (S_c) of 21 and 42 m/s show a fully monophasic AlNi structure. With the increase of cooling rate, the as-spun and annealed ribbons with 42 m/s show a higher (100) orientation factor $F_{(100)}$, which is related to the lower barrier to recrystallization than the ribbons with 21 m/s. Furthermore, the ribbons with a higher orientation factor $F_{(100)}$ demonstrate a higher corrosion resistance, as deduced from electrochemical and immersion tests.

(2) The passive film of the as-spun ribbon with 21 m/s has three oxide layers, after annealing at 700 °C, the Al_2O_3 layer (Region I) transforms into a loose and porous layer, which has low corrosion resistance. In contrast, the passive film of the as-spun and annealed ribbons with 42 m/s contains a stable and compact Al_2O_3 + AlNi passive film in the inner layer (Region II). Hence, the corrosion resistance of $Al_{50}Ni_{50}$ alloy can be improved by increasing S_c plus annealing, thereby offering a new strategy to stably passivate Al- or Ni-based alloys.

CRediT authorship contribution statement

Han-ze LIU: Conceptualization, Methodology, Validation, Data curation, Investigation, Formal analysis, Writing – Original draft, Writing – Review & editing, Funding acquisition; **Zhi-cheng YAN:** Methodology, Formal analysis; **Qi CHEN:** Formal analysis, Writing – Review & editing; **Hao ZHANG:** Methodology, Validation; **Yu FENG:** Methodology, Formal analysis. **Zhi-gang QI:** Writing – Review & editing; **Zhao-xuan WANG:** Writing – Review & editing; **Shao-peng PAN:** Methodology, Formal analysis; **Yi-yong JIA:** Methodology, Validation; **Wei-min WANG:** Conceptualization, Formal analysis, Writing – Review & editing, Supervision, Funding acquisition.

Declaration of competing interest

The authors declare that they have no known competing financial interests or personal relationships that could have appeared to influence the work reported in this paper.

Acknowledgments

This work was financially supported by the Key Research and Development Program of China (No. 2022YFB2404102), the National Natural Science Foundation of China (Nos. 51971093, 52171158), and the Key Research and Development Program of Shandong Province, China (Nos. 2021ZLGX01, 2022CXGC020308).

References

[1] ATZMON M. Characterization of AlNi formed by a self-sustaining reaction during mechanical alloying [J]. Materials Science and Engineering: A, 1991, 134: 1326−1329.

[2] NGUYEN-TRONG D, NGUYEN-TRI P. Factors affecting the structure, phase transition and crystallization process of AlNi nanoparticles [J]. Journal of Alloys and Compounds, 2020, 812: 152133.

[3] MORSI K. Review: Reaction synthesis processing of Ni−Al intermetallic materials [J]. Materials Science and Engineering: A, 2001, 299(1/2): 1−15.

[4] DAOUD A, ABO-ELKHAR M. Influence of Al_2O_3 or ZrO_2 particulate addition on the microstructure aspects of AlNi and AlSi alloys [J]. Journal of Materials Processing Technology, 2002, 120(1/2/3): 296−302.

[5] GAO Hai-yan, HE Yue-hui, ZOU Jin, XU Nan-ping, LIU C T. Tortuosity factor for porous FeAl intermetallics fabricated by reactive synthesis [J]. Transactions of Nonferrous Metals Society of China, 2012, 22(9): 2179−2183.

[6] OHTSU N, OKU M, OBARA K, ITO S, SHISIDO T, WAGATSUMA K. Oxidation behavior of NiAl alloy at low temperatures [J]. Surface and Interface Analysis, 2007, 39(6): 528−532.

[7] RODRIGUES A V, LIMA T S, VIDA T A, BRITO C, GARCIA A, CHEUNG N. Microstructure features and mechanical/electrochemical behavior of directionally solidified Al−6wt.%Cu−5wt.%Ni alloy [J]. Transactions of Nonferrous Metals Society of China, 2021, 31(6): 1529−1549.

[8] CHEN H, ZHANG Z, HAO X H, HUANG B X, ZHAO X C, HU C C. Microstructure and tribocorrosion properties of NiTi/$AlNi_2Ti$ ternary intermetallic alloy [J]. Vacuum, 2021, 184: 109928.

[9] TURRILLAS X, MAS-GUINDAL M J, HANSEN T C, RODRIGUEZ M A. The thermal explosion synthesis of AlNi monitored by neutron thermodiffractometry [J]. Acta Materialia, 2010, 58: 2769−2777.

[10] CHEREPANOV P V, MELNYK I, ANDREEVA D V. Effect of high intensity ultrasound on Al_3Ni_2, Al_3Ni crystallite size in binary AlNi (50 wt.% of Ni) alloy [J]. Ultrasonics Sonochemistry, 2015, 23: 26−30.

[11] GEORGE E P, LIU C T, HORTON J A, SPARKS C J, KAO M, KUNSMANN H, KING T. Characterization, processing, and alloy design of NiAl-based shape memory alloys [J]. Materials Characterization, 1994, 32(3): 139−160.

[12] LAVERNIA E J, AYERS J D, SRIVATSAN T S. Rapid solidification processing with specific application to aluminium alloys [J]. International Materials Reviews, 1992, 37(1): 1−44.

[13] FANG Jun, ZHONG Yong-hui, XIA Ming-kuang, ZHANG Feng-wei. Mechanical and thermo-physical properties of rapidly solidified Al−50Si−Cu(Mg) alloys for thermal management application [J]. Transactions of Nonferrous Metals Society of China, 2021, 31(3): 586−594.

[14] INOUE A, KIMURA H. Fabrications and mechanical properties of bulk amorphous, nanocrystalline, nano-quasicrystalline alloys in aluminum-based system [J]. Journal of Light Metals, 2001, 1(1): 31−41.

[15] LAVERNIA E J, SRIVATSAN T S. The rapid solidification processing of materials: Science, principles, technology, advances, and applications [J]. Journal of Materials Science, 2010, 45(2): 287−325.

[16] EL-ESKANDARANY M S. Introduction [M]// Mechanical Alloying. Oxford; William Andrew Publishing, 2015: 1−12.

[17] JIA Yi, LIU Zhi-dong, LI Sha, YAO Hao-ming, REN Zhong-kai, WANG Tao, HAN Jian-chao, XIAO Shu-long, CHEN Yu-yong. Effect of cooling rate on solidification microstructure and mechanical properties of TiB_2-containing TiAl alloy [J]. Transactions of Nonferrous Metals Society of China, 2021, 31(2): 391−403.

[18] MŁYNAREK-ŻAK K, WIERZBICKA-MIERNIK A, KĄDZIOŁKA-GAWEŁ M, CZEPPE T, RADOŃ A, BABILAS R. Electrochemical characterization of rapidly solidified Al−(Cr,Cu,Ni,Y,Zr)−Fe alloys [J]. Electrochimica Acta, 2022, 409: 139836.

[19] WU Yi-you, ZHANG Tao-mei, CHEN Chao, HOSSEINI S R E, ZHANG Xiao-yong, ZHOU Ke-chao. Microstructure and mechanical property evolution of additive manufactured eutectic Al−2Fe alloy during solidification and aging [J]. Journal of Alloys and Compounds, 2022, 897: 163243.

[20] YAO Qing-rong, TANG Ying, ZHOU Huai-ying, DENG Jian-qiu, WANG Zhong-min, PAN Shun-kang, RAO Guang-hui, ZHU Qi-ming. Effect of rapid solidification treatment on structure and electrochemical performance of low-Co AB5-type hydrogen storage alloy [J]. Journal of Rare Earths, 2014, 32(6): 526−531.

[21] POON S J, SHIFLET G J, GUO F Q, PONNAMBALAM V. Glass formability of ferrous- and aluminum-based structural metallic alloys [J]. Journal of Non-Crystalline Solids, 2003, 317(1/2): 1−9.

[22] VISHWANADH B, JO J, BONIFACIO C S, WIEZOREK J M K. Site-specific preparation of plan-view samples with large field of view for atomic resolution STEM and TEM studies of rapidly solidified multi-phase AlCu thin films [J]. Materials Characterization, 2022, 189: 111943.

[23] UMIROV N, SEO D H, KIM T, KIM H Y, KIM S S. Microstructure and electrochemical properties of rapidly solidified Si−Ni alloys as anode for lithium-ion batteries [J]. Journal of Industrial and Engineering Chemistry, 2019, 71: 351−360.

[24] NAPOLITANO R E, MECO H. The role of melt pool behavior in free-jet melt spinning [J]. Metallurgical and Materials Transactions A, 2004, 35(5): 1539−1553.

[25] MS M, STUTTGART B CL, HAEBNER F, VERLAG D R. Recrystallization of metallic material [M]. Stuttgart: Riederer-Verlag, 1978: 251−79.

[26] LENG Jin-feng, REN Bing-hui, ZHOU Qing-bo, ZHAO Ji-wei. Effect of Sc and Zr on recrystallization behavior of 7075 aluminum alloy [J]. Transactions of Nonferrous Metals Society of China, 2021, 31(9): 2545−2557.

[27] LI Xin-yu, XIA Wei-jun, CHEN Ji-hua, YAN Hong-ge, LI Zhen-zhen, SU Bin, SONG Min. Dynamic recrystallization, texture and mechanical properties of high Mg content Al−Mg alloy deformed by high strain rate rolling [J]. Transactions of Nonferrous Metals Society of China, 2021, 31(10): 2885−2898.

[28] GARDNER K J, GRIMES R. Recrystallization during hot deformation of aluminium alloys [J]. Metal Science, 1979, 13(3/4): 216−222.

[29] LEE S L, CHIU Y C, PAN T A, CHEN M C. Effects of trace amounts of Mn, Zr and Sc on the recrystallization and corrosion resistance of Al−5Mg alloys [J]. Crystals, 2021, 11: 926.

[30] DOCHE M L, RAMEAU J J, DURAND R, NOVEL-CATTIN F. Electrochemical behaviour of aluminium in concentrated NaOH solutions [J]. Corrosion Science, 1999, 41(4): 805−826.

[31] EMREGÜL K C, AKSÜT A A. The behavior of aluminum in alkaline media [J]. Corrosion Science, 2000, 42(12): 2051−2067.

[32] TREACY G M, BRESLIN C B. Electrochemical studies on single-crystal aluminium surfaces [J]. Electrochimica Acta, 1998, 43(12/13): 1715−1720.

[33] WANG He-zu, YANG Wen-guang, ZHANG Bo-wei, ZHANG Zhan, WU Cong, WU Jun-sheng. Effect of crystal orientation on the corrosion behavior of as-cast pure aluminum anodes in air batteries [J]. Journal of Materials Engineering and Performance, 2022, 31(5): 3584−3593.

[34] ISASI J A, METZGER M. Structure-dependent corrosion of high-purity Al in HNO_3 and H_2SO_4 [J]. Corrosion Science, 1971, 11: 631−639.

[35] ZHOU Yu. Materials analysis and testing technology [M]. Harbin: Harbin Institute of Technology Press, 2007. (in Chinese)
[36] LOTGERING F K. Topotactical reactions with ferrimagnetic oxides having hexagonal crystal structures—I [J]. Journal of Inorganic and Nuclear Chemistry, 1959, 9(2): 113−123.
[37] PEI Hai-qing, LI Meng, WANG Ping, YAO Xiao-hu, WEN Zhi-xun, YUE Zhu-feng. The effect of tensile stress on oxidation behavior of nickel-base single crystal superalloy [J]. Corrosion Science, 2021, 191: 109737.
[38] XU Hui, SHEN Ke-chang, LIU Shuai, ZHANG Lai-chang, WANG Xiao-guang, QIN Jing-yu, WANG Wei-min. High activity methanol/H_2O_2 catalyst of nanoporous gold from Al–Au ribbon precursors with various circumferential speeds [J]. The Journal of Physical Chemistry C, 2016, 120(44): 25296−25305.
[39] KAWASAKI T, TANAKA H. Formation of a crystal nucleus from liquid [J]. Proceedings of the National Academy of Sciences, 2010, 107: 14036−14041.
[40] SWAMY V T, RANGANATHAN S, CHATTOPADHYAY K. Rapidly solidified Al−Cr alloys: Crystalline and quasicrystalline phases [J]. Journal of Materials Research, 1989, 4(3): 539−551.
[41] BOLZONI L, HARI BABU N. Engineering the heterogeneous nuclei in Al−Si alloys for solidification control [J]. Applied Materials Today, 2016, 5: 255−259.
[42] OHASHI T, FUKATSU N, ASAI K. Crystallization and precipitation structures of quasicrystalline phase in rapidly solidified Al−Mn−X ternary alloys [J]. Journal of Materials Science, 1989, 24(10): 3717−3724.
[43] BOLZONI L, XIA Ming-xu, BABU N H. Formation of equiaxed crystal structures in directionally solidified Al−Si alloys using Nb-based heterogeneous nuclei [J]. Scientific Reports, 2016, 6(1): 39554.
[44] ZHANG Cheng, ZHU Chao-yi, SHIN S, VECCHIO K. Enhancement of 〈001〉 recrystallization texture in non-equiatomic Fe−Ni−Co−Al-based high entropy alloys by combination of annealing and Cr addition [J]. Journal of Alloys and Compounds, 2018, 768: 277−286.
[45] BENCHABANE G, BOUMERZOUG Z, THIBON I, GLORIANT T. Recrystallization of pure copper investigated by calorimetry and microhardness [J]. Materials Characterization, 2008, 59(10): 1425−1428.
[46] ČEKEREVAC M, SIMIČIĆ M, BUJANOVIĆ L N, POPOVIĆ N. The influence of silicate and sulphate anions on the anodic corrosion and the transpassivity of iron and silicon-rich steel in concentrated KOH solution [J]. Corrosion Science, 2012, 64: 204−212.
[47] ZHANG Yuan-jie, SONG Bo, MING Jun, YAN Qian, WANG Min, CAI Chao, ZHANG Cheng, SHI Yu-sheng. Corrosion mechanism of amorphous alloy strengthened stainless steel composite fabricated by selective laser melting [J]. Corrosion Science, 2020, 163: 108241.
[48] LUO Hong, SU Huai-zhi, DONG Chao-fang, LI Xiao-gang. Passivation and electrochemical behavior of 316L stainless steel in chlorinated simulated concrete pore solution [J]. Applied Surface Science, 2017, 400: 38−48.
[49] LAMAKA S V, SHCHUKIN D G, ANDREEVA D V, ZHELUDKEVICH M L, MÖHWALD H, FERREIRA M G S. Sol−gel/polyelectrolyte active corrosion protection system [J]. Advanced Functional Materials, 2008, 18: 3137−3147
[50] SONG G, ATRENS A, JOHN D S, WU X, NAIRN J. The anodic dissolution of magnesium in chloride and sulphate solutions [J]. Corrosion Science, 1997, 39(10/11): 1981−2004.
[51] SONG Guang-ling, UNOCIC K A. The anodic surface film and hydrogen evolution on Mg [J]. Corrosion Science, 2015, 98: 758−765.
[52] XU Jiang, LIU Lin-lin, LI Zheng-yang, MUNROE P, XIE Zong-han. Niobium addition enhancing the corrosion resistance of nanocrystalline Ti_5Si_3 coating in H_2SO_4 solution [J]. Acta Materialia, 2014, 63: 245−260.

增大冷速和退火对 $Al_{50}Ni_{50}$ 合金耐蚀性能的改善

刘瀚泽[1]，闫芝成[1]，陈 其[1]，张 昊[1]，冯 玉[1]，齐志港[1]，王兆萱[1]，潘少鹏[2]，贾义勇[3]，王伟民[1]

1. 山东大学 材料科学与工程学院 材料液固结构演变与加工教育部重点实验室，济南 250061；
2. 太原理工大学 材料科学与工程学院，太原 030002；
3. 华美新材料(菏泽)有限公司，菏泽 274000

摘 要：通过周向速度(S_c)分别为 21 和 42 m/s 的熔带甩带法制备单相 $Al_{50}Ni_{50}$ 条带，然后采用多种实验方法研究在不同温度下退火 $Al_{50}Ni_{50}$ 条带的显微组织和腐蚀行为。随着 S_c 从 21 m/s 提高到 42 m/s，相应的铸态和退火条带的(100)晶体取向因子 $F_{(100)}$增大，再结晶的障碍减少以及钝化膜的总电阻增大。S_c=42 m/s 的铸态条带比 21 m/s 的铸态和退火的条带具有更稳定、更致密的 Al_2O_3 钝化膜，并可以通过在 700 ℃退火进一步提升。因此，提高冷却速率和选择适当温度进一步退火可以提高 AlNi 条带的耐腐蚀性能。

关键词：AlNi 合金；快速凝固；取向因子；再结晶；腐蚀性为

(Edited by Xiang-qun LI)